Advanced Intelligent Systems

ADVANCED INTELLIGENT SYSTEMS Open Access

www.advintellsyst.com

RESEARCH ARTICLE OPEN ACCESS

Small-Scale Magnetic Peristaltic Soft Robot With Mobility and Transport Capabilities

Mohammad Hasan Dad Ansari[1,2] | Linda Paternò[1,2] | Chenjun Wu[1,2] | Veronica Iacovacci[1,2] |
Arianna Menciassi[1,2]

[1]The BioRobotics Institute, Scuola Superiore Sant'Anna, Pontedera, Italy | [2]Department of Excellence in Robotics & AI, Scuola Superiore Sant'Anna, Pontedera, Italy

Correspondence: Chenjun Wu (chenjun.wu@santannapisa.it) | Arianna Menciassi (arianna.menciassi@santannapisa.it)

Received: 11 January 2026 | **Revised:** 5 June 2026 | **Accepted:** 12 June 2026

Keywords: magnetic robots | peristalsis | small-scale | soft robots

ABSTRACT

Peristaltic locomotion and transport are fundamental biological mechanisms used in soft-bodied organisms (e.g., earthworms) and anatomical structures (e.g., the gastrointestinal tract) to generate axial movement through coordinated muscle contractions. However, bioinspired multipurpose peristaltic systems for both locomotion and transport remain underexplored. This work presents a small-scale, lightweight, untethered, fully soft magnetic robot that locomotes in different environments and transports cargo within its hollow body. It is composed of eight 1-mm-thick and 30 mm long elastomeric strips featuring helical magnetization profiles, generating peristaltic waves under uniform rotating magnetic fields (10–80 mT, 1–5 Hz). A coupled magneto-mechanical finite-element model numerically predicts the robot's deformation and is experimentally validated (RMSE ≈ 1 mm). Robot capabilities are demonstrated through locomotion over solid cylindrical rods, reaching peak speeds of 33.45 mm min^{-1} (≈1.1 body lengths min^{-1}), and inside narrow lumina, yielding speeds up to 124.17 mm min^{-1} (≈4.1 body lengths min^{-1}). Peristaltic cargo transport of solid spheres and cylindrical rods within its lumen is also demonstrated. Multifunctional demonstrations combining cargo transport and locomotion, including bridging lumina gaps, are also reported. The robot's soft, lightweight, and untethered design allows operation in complex environments without embedded power sources, enabling several potential biomedical and industrial applications.

1 | Introduction

Bioinspired robotics seeks to replicate the efficiency and adaptability of living organisms, drawing inspiration from the embodied intelligence of their anatomical structures, which enables them to perform and adjust to diverse and unstructured environments. In this regard, the musculoskeletal structures of animals have become a primary source of inspiration for the development of robots with enhanced versatility and robustness in real-world applications [1].

Locomotion in animals occurs through a wide range of movement strategies, each activated by precisely evolved anatomical structures and adapted to specific environments and functional demands [2–4]. One such strategy involves peristalsis, which is exploited by soft-bodied organisms like earthworms to crawl and burrow efficiently [5]. This type of locomotion relies on the presence of a hydrostatic skeleton, where internal fluid pressure provides structural support, enabling the coordinated contraction and relaxation of muscles to generate movement. Since peristalsis is characteristic of animals with a musculoskeletal system that lacks rigid structures, it represents a particularly valuable principle in soft robotics. Apart from locomotion, peristaltic movements of muscles are also a fundamental biological mechanism vital for numerous functions in animals and humans. Peristalsis enables transportation of substances such as food and fluids through rhythmic contraction waves propagating along tubular soft structures, such as the esophagus, stomach, and intestines [6–8]. This ability of peristalsis to facilitate locomotion and transport has inspired the development of different robotic systems, demonstrating how the same movement strategy can be adapted to meet diverse functional demands.

In literature, peristalsis has been achieved using shape memory alloys (SMA), tendon-driven, motor-driven, pneumatic, piezoelectric, light-driven, or magnetic actuation. One of the earliest examples of peristaltic robots was a multisegment robot actuated using SMA springs. Each segment had an SMA spring that contracted longitudinally when heated, causing radial expansion of the silicone shell. Upon cooling, the shell elasticity restored its shape. The Meshworm used a similar approach, with coiled SMA actuators around a braided mesh structure, enabling segmented contraction and relaxation to replicate earthworm-like undulatory locomotion [9, 10]. SMA actuators have also been reported combined with tensegrity structures acting as individual segments [11]. SMA actuation suffers from a low response time and is inefficient as significant energy is lost through heating. Although SMA-based solutions are often tethered, battery-powered options could enable untethered operation, though this would increase the bulkiness of the robot [9]. Tendon-driven peristaltic actuation has been shown on Softworm which is a robot made of a continuously deformable mesh for pipe-inspection. Individual segments of the robot can contract radially and expand longitudinally upon pulling of the corresponding cables to translate the robot [12, 13]. While tendon-driven actuation can achieve faster response time, it requires complex routing and suffers from friction and backlash. The need for intricate routing and multiple strings also makes fabrication more complex. Additionally, tendon-driven systems suffer from being tethered, limiting their reach for remote environments. Zhang et al. demonstrated peristaltic robots that utilize multisegment Sarrus linkage modules and cylindrical motor-cam-driven transmission systems to achieve earthworm-inspired burrowing and locomotion for underwater archaeological sampling. While such system improves structural strength of the robot, it is bulky, complex, challenging to be scaled-down, and tethered [14]. Pneumatic peristaltic soft robots were demonstrated by Nakamura et al. who used cylindrical actuators able to contract longitudinally and expand radially upon pressurization. Multiple actuators were arranged coaxially with a tension spring along the axis acting as an endoskeleton and building up a complete peristaltic robot [15]. Similarly, pneumatic peristaltic robots have been shown for multiterrain crawling, pipeline inspection, and intestine inspection [16–18]. By programming the pressure profile of each segment, such robots can move in different media and in confined spaces [15, 16]. While all the above examples have no working channels, which prevents them from carrying cargo, other peristaltic soft robots have been shown for transport applications. Suzumori et al. and Uzawa et al. demonstrated segmented pneumatic systems capable of cargo transport [19, 20]. While pneumatic systems are compliant, they also need tethered tubing which makes the robot bulky and prone to leakage, thus significantly limiting the feasibility of miniaturized, untethered systems.

Bio-inspired intestine robots have been demonstrated that utilize coupled rotational-contraction dynamics of antagonistic chiral Kresling origami structures and unidirectional valves to achieve directional transport through peristaltic motion. The system achieves high transport speeds, large payload capacity, and stable operation across varying inclinations, but the dependence on a servo-driven mechanism for wave propagation makes it difficult to be miniaturized or untethered [21]. Piezoelectric peristaltic micropumps have been demonstrated that utilize traveling waves on polymer membranes to transport liquids [22]. In contrast to SMA, tendon-driven, and pneumatic solutions, piezoelectric actuators can be sub-cm scale but require a bulky control and powering system [23]. While they have fast response times and high precision, they suffer from being tethered and with limited deformation, and they require very high driving voltages. In the attempt to go towards untethered soft peristaltic robots, a light-driven device was demonstrated by Xia et al. using smart hydrogels, capable of directional transport of liquids [24]. In another work, Palagi et al. proposed a soft microrobot made of liquid-crystal elastomers driven by structured monochromatic light and able to generate traveling-wave motions to self-propel [25]. While light-driven solutions can be untethered, lightweight, and sub-cm scale, they still require a line of sight, complicated lighting systems and they can suffer from slow response time.

In this context, magnetic actuation stands as a promising alternative approach, especially for locomotion in confined and complex environments, as it enables untethered operation with an off-board power source [26–30]. Additionally, magnetic solutions can also be lightweight, simple to fabricate, and show programmable large shape transformations [26, 31]. For instance, Wen et al. recently demonstrated magnetoactive bistable soft actuators capable of large, programmable shape transformations under low magnetic fields, leading to a promising energy efficient multifunctional magnetic soft robotic system [31]. An example of magnetic peristaltic robot was demonstrated by Dong et al. to transport viscous fluids and solid cargo. Soft sheets composed of magnetic cilia that produced an undulating motion were attached to the inner wall of a tubular structure. By synchronizing the motion of the cilia along the length of the robot, a peristaltic wave is generated that transports cargo within the tube [32]. Even though this design proves to be particularly interesting, it cannot be exploited for locomotion, as the peristaltic movement is restricted to the internal surface of the robot, limiting its adaptability and its capability to respond to different functional demands. Another example of a magnetic peristaltic robot was introduced by Zhang et al. who demonstrated an intestine-inspired tubular magnetic soft peristaltic pump, providing only preliminary, gravity-assisted demonstrations of liquid and cargo transport [33]. Additionally, this solution is particularly tedious to fabricate due to the voxel-by-voxel assembly process, which requires specialized and expensive machinery to achieve the tailored magnetization profile. While these two studies show the capability of magnetic peristaltic soft robots at the cm [32] and mm [33] scales, they remain limited to transport tasks, without addressing the potential of peristalsis for robot locomotion. As evident from Table 1, none of the existing studies have achieved a truly multipurpose system capable of effectively and seamlessly merging locomotion and transport within a single solution. Moreover, none of the locomotion studies have yet shown locomotion on rods. This limitation arises either from the absence of a free working channel due to bulky actuation mechanisms or the need for stable anchorages that restrict free movement. To overcome this gap, we propose a magnetic peristaltic robot that leverages frictional interactions with the surroundings to achieve both locomotion across different environments through a bio-inspired approach and cargo

TABLE 1 | Summary of state-of-the-art peristaltic robots. The ability to perform locomotion and transport and the need to have tethers/line of sight are highlighted for different peristaltic robot examples in the literature.

Study	Actuation technology	Untethered/no line of sight	Locomotion	Transport
[9]	SMA	No	Yes	No
[10]	SMA	No	Yes	No
[11]	SMA/tensegrity structures	No	Yes	No
[12, 13]	Tendons	No	Yes	No
[14]	Sarrus-linkage/cam driven	No	Yes	No
[15]	Pneumatic	No	Yes	No
[16]	Pneumatic	No	Yes	No
[17]	Pneumatic	No	Yes	No
[18]	Pneumatic	No	Yes	No
[19]	Pneumatic	No	No	Yes
[20]	Pneumatic	No	No	Yes
[21]	Origami/motor	No	No	Yes
[22]	Piezoelectric	No	No	Yes
[24]	Light	No	No	Yes
[25]	Light	No	Yes	No
[32]	Magnetic	Yes	No	Yes
[33]	Magnetic	Yes	No	Yes
Present	Magnetic	Yes	Yes	Yes

transport leveraging a hollow cylindrical body. The robot is made of 8 thin sheets of soft magnetic material, each having a spiral magnetization profile along its length, and assembled side-by-side using soft silicone spacers. The magnetization profile, as reported in the literature, enables the formation of peristaltic waves along the length of the robot [33]. The result is a fully soft, hollow cylindrical structure that is untethered and lightweight, offering an efficient and versatile solution with a unique combination of multifunctionality, robustness, and fabrication simplicity. Our jig-assisted magnetization method enables the generation of truly continuous spiral magnetization profiles through a substantially simpler and lower-cost manufacturing strategy, compared to fabrication solutions proposed in literature [33]. Furthermore, through smart exploitation of friction, the proposed robot exhibits robust locomotion both on rods and within luminal environments and is able to transport solid objects. This work is further supported by comprehensive numerical modeling of both the overall robot behavior and its individual constituent components.

2 | Results and Discussion

2.1 | Peristaltic Robot

The peristaltic robot (Figure 1) was 30 mm in length and 9 mm in diameter with a 7 mm diameter lumen. An example helical magnetization profile within one of the eight soft magnetic composite strips is shown in Figure 1B. The starting direction of the helical magnetization profile at the top end of the whole robot is illustrated on the left side of Figure 1C. When a magnetic field is applied along the *Y*-axis, the top end contracts along the *Y*-axis and expands along the *X*-axis, creating a constriction. If the magnetic field is now rotated, the entire robot also rotates or rolls on the surface, as the robot essentially acts as a single magnetic domain in this case. However, if the robot is prevented from rotation (e.g., by friction), the constriction formed at the top, indicated by black arrows in Figure 1D, propagates along the robot length in the −Z direction when the applied magnetic field (red arrows) rotates in the X–Y plane along the +Z direction, thus generating a peristaltic wave. Conversely, rotating the magnetic field in the −Z direction causes the peristaltic wave to travel in the +Z direction. For a complete wave formation in the robot as shown in Figure 1D, one full twist of the helical magnetization profile along the length (L) is required (twist angle of 360° L^{-1}). This ensures continuous peristaltic motion of the robot with continuous rotation of the magnetic field acting uniformly along the entire length of the robot. Using this motion, the robot can both locomote and transport cargo (Figure 1E).

Each twisting unit produces a longitudinal twist when actuated. The behavior of the strips was modeled and experimentally validated in terms of their twist angle under varying magnetic field strength. The magnetic field induced torques on the twisting unit were modeled as opposing tangential stresses on its boundaries (Figure S1). Such distributed magnetic torques, which are difficult to represent directly in conventional continuum mechanics, were first approximated in previous work by discretizing each robot into ten equal magnetized elements [34]. Then, a refined torque-mapping formulation that offers substantially improved accuracy was subsequently developed [35]. The results indicate that the model successfully captures the behavior of the twisting

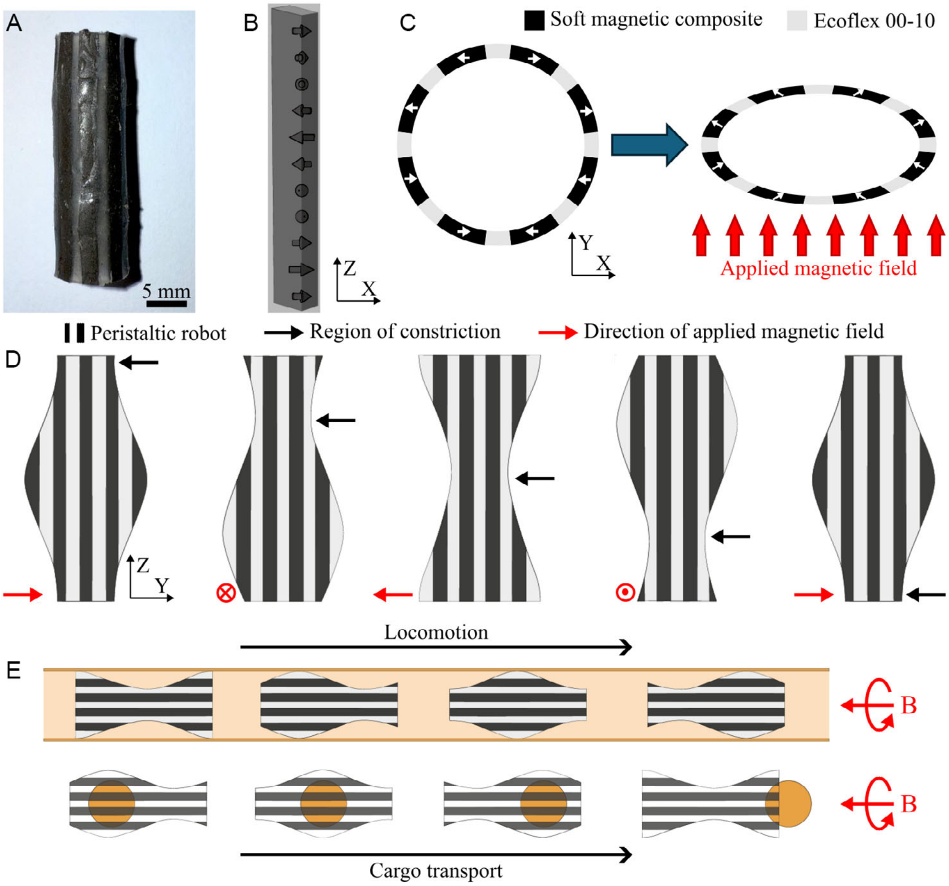

FIGURE 1 | Small-scale magnetic peristaltic robot concept and working principle. (A) Peristaltic robot prototype. (B) Example of helical magnetization profile in one of the magnetic composite strips. The arrows within the strip indicate the direction of magnetization. (C) When a magnetic field is applied along Y, the top-most layer of the robot constricts. (D) If the robot is prevented from rolling, this constriction travels along the robot body when a uniform rotating field is applied. The direction of rotation of the magnetic field, which acts uniformly along the entire body of the robot, is shown in red following the right hand rule. (E) The robot can be used for locomotion and cargo transport applications.

units, accurately predicting the numerical values and the trend in twist angles as the magnetic field strength increases (Figure S2).

The behavior of the complete robot, which is a combination of twisting units (Figure 2), was similarly modeled under varying rotating magnetic field strengths. The induced torques on the robot used for the model are shown in Figure S3. As with a single twisting unit, the robot was fixed at one end, and identical boundary conditions were applied in the simulation. However, unlike single twisting units, the complete robot shows peristalsis. To validate the model, the robot prototype was actuated with the magnetic fields rotating in the X–Y plane, perpendicular to the robot axis. The shape of the robot in the Y–Z plane was captured using a camera. Figure 2A shows a comparison of the experimentally captured shapes with those generated by the model at fields along X, Y, –X, and –Y directions at a strength of 30 mT. The position of the narrowest section in the robot from the fixed end was derived experimentally and compared with the values from the model in Figure 2B. It is worth noting here that even if the absolute minima for narrowest width occurs at the top end when the field is applied in the –X direction, there is a local minima at a position 24.13 mm from the fixed end, indicating that the constriction has indeed traveled down from the top-end. The deformation of the free end was also recorded using a camera. Figure 2C shows a comparison of the experimentally captured shapes with those generated by the model at four field orientations at a strength of 30 mT. For numerical validation, the constriction length of the free end along the X-axis measured from experimental images was compared with model predictions. As shown in Figure 2B,D, the model accurately predicts the robot shape changes across magnetic field strengths and orientations. The root mean square error (RMSE) between the experiments and simulation in all four directions was found to be very low, just 1.02 mm for narrowest width position (Figure 2B), and at most 0.75 mm observed in case of 20 mT field strength for constriction length (Figure 2D). The model also predicts wall contact at 35 mT when the field is applied in the -Y direction, which was also observed experimentally.

Peristaltic locomotion relies on the propagation of rhythmic contraction waves along the body. Depending on how friction is modulated during the contraction phase, the resulting movement can either oppose or align with the direction of wave propagation. Without anchoring, the robot would simply rotate as if it was a single magnetic dipole. Anchoring through friction not only prevents the entire robot from rotating but also provides a stable point against which the body can push, thus enabling forward locomotion. The direction of movement depends on where the anchoring

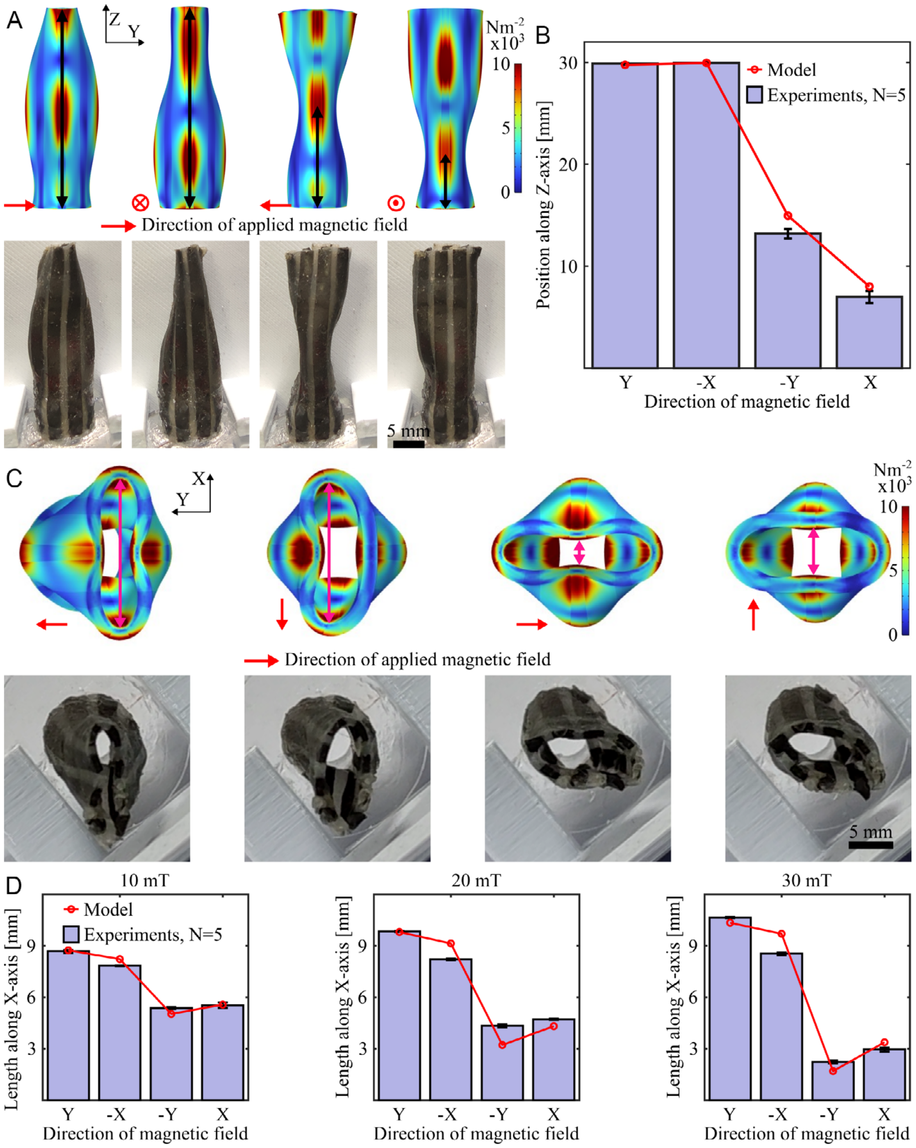

FIGURE 2 | Model and experimental validation of the peristaltic behavior of the robot fixed at one end. (A) A comparison of the deformation of the robot between the model prediction and experiments in Y–Z plane, when a magnetic field (30 mT) is applied as shown by red arrows. (B) The position of narrowest width along Z-axis (shown with black arrows in (A) for varying magnetic field strengths and directions compared between model prediction and experiments ($N = 5$). Scale bar: 5 mm. (C) A comparison of the deformation of the free end of the robot when a magnetic field (30 mT) is applied as shown by red arrows between the model prediction and experiments. (D) The constriction length along X-axis (shown with pink arrows in (C) for varying magnetic field strengths and directions compared between model prediction and experiments ($N = 5$). Scale bar: 5 mm.

occurs relative to the peristaltic wave [36]. When anchoring (friction) takes place in contracted regions, the body moves opposite to the direction of wave propagation (friction-enhancing model). On the other hand, when anchoring takes place in expanded regions, the body moves along the direction of wave propagation (friction-reducing model). This behavior has been exploited to control the direction of robot peristaltic motion depending on whether it moves on a cylindrical rod or within a narrow lumen (Figure 3). The peristaltic robot moves opposite to the direction of peristaltic wave over the rod (Figure 3A, anchoring at contracted regions) and in the direction of the peristaltic wave inside the lumen (Figure 3B, anchoring at expanded regions). This behavior illustrates the critical role of friction in controlling peristaltic locomotion and highlights robot physical intelligence in adapting to different environmental conditions or functional needs.

2.2 | Locomotion of the Peristaltic Robot

The magnetic robot was able to locomote over rigid cylindrical rods (Figure 4). A 6 mm rod diameter was chosen because it increased the frictional interaction between the actuated robot and the rod, thus suppressing rolling. Instead, it gave rise to longitudinal peristaltic waves which resulted in locomotion of the robot (Figure 4A and Movie S1). An example of distance traveled by the robot over a rod 3D printed with Biomed Clear resin (Formlabs), tracked and plotted against time is given in Figure 4B. A linear fit on this data resulted in R^2 of 0.999 which confirmed the steady, constant speed of locomotion. The robot achieved a similar average speed of just over 6 mm min^{-1} (approximately 0.2 body lengths min^{-1}) across different rod materials (Biomed Clear, PET-G, PLA) when driven by a 70 mT field rotating at 1 Hz (Figure 4C). Its ability to move

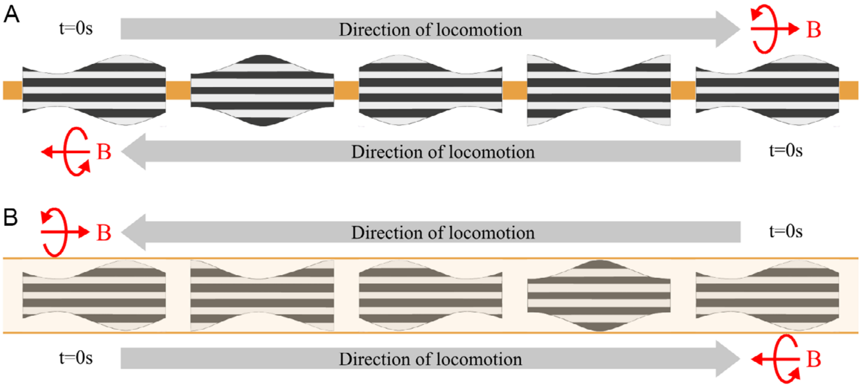

FIGURE 3 | Dependance of locomotion direction on the robot region experiencing friction. $t = 0$ s indicates the initial time when the robot starts moving. The figure illustrates how the same direction of rotation of magnetic field results in the same temporal sequence of shape changes but results in locomotion in opposite directions in the two different configurations, i.e., over the rod (A) or inside a lumen (B). (A) When the robot travels over a rod of 6 mm diameter, friction acts on its contracted area and the locomotion is in the opposite direction as the peristaltic wave. (B) When the robot travels inside a hollow lumen, friction acts on its expanded area and the locomotion is in the same direction as the peristaltic wave.

effectively over substrates with varying coefficients of friction (see Supporting Information) demonstrates robust peristaltic locomotion across diverse surface conditions. The possible combinations of magnetic field strength and rotation frequency provided by the electromagnetic actuation system are listed in Table S3. For each of the possible actuation conditions, the resulting locomotion speed was measured (Table S4) and plotted in Figure 4D. Locomotion speed increases both with increasing magnetic field frequency and strength consistent with the state of the art theoretical predictions [36]. Locomotion speed grows with driving frequency because higher frequency generates more peristaltic cycles per unit time and therefore greater net displacement per unit time, provided the body can still follow the imposed frequency. It is also predicted that the speed starts plateauing and does not increase indefinitely.

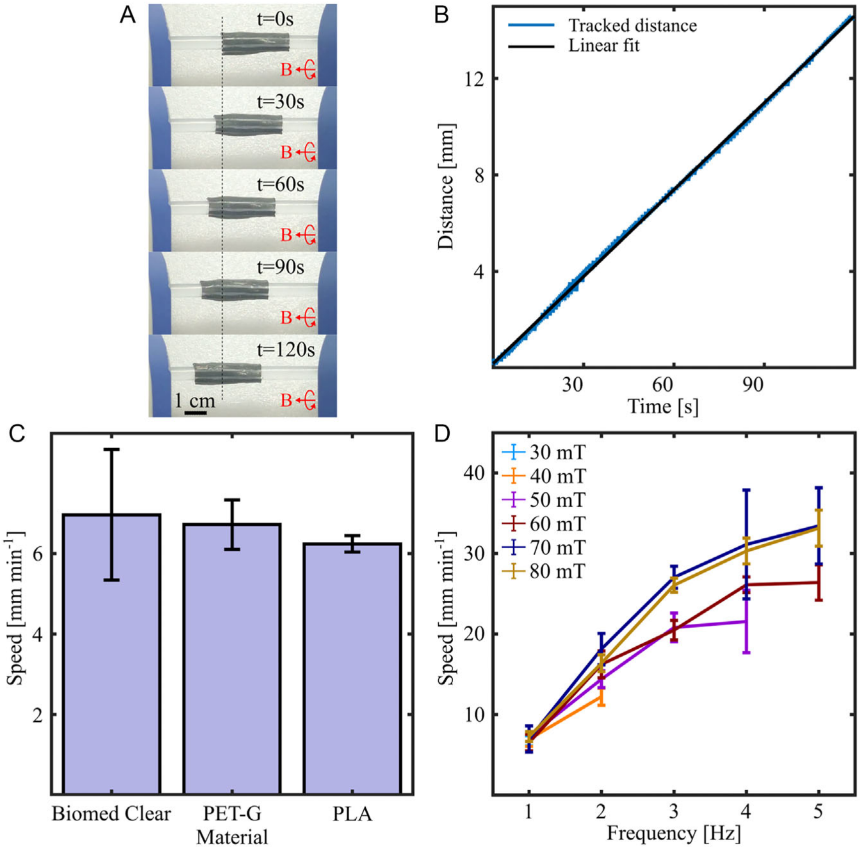

FIGURE 4 | Linear locomotion of the peristaltic robot over a cylindrical rod of 6 mm diameter under rotating magnetic fields (70 mT, 1 Hz). (A) Timestamped sequence of images showing the steady movement of the robot over a BiomedClear rod. (B) Distance traveled by the robot over a BiomedClear rod plotted against time (70 mT, 1 Hz). A linear fit resulted in R^2 of 0.999. (C) Robot speed comparison over 6 mm rods made from different materials ($N = 5$). (D) Robot speed comparison on a 6 mm BioMedClear rod with different magnetic field strengths and rotational frequencies ($N = 5$).

In our experiments, we observe such behavior through asynchronous motion especially at low field strengths as the plateauing occurs at lower frequencies (Table S3). It is possible that such asynchronous behavior at higher field strengths may occur at frequencies beyond the limits of our field generator. Furthermore, the peristaltic wave amplitude depends on the magnetic field strength (Figure 2). However, due to the presence of the rod, increasing the field only slightly enhances deformation of the robot, leading to a modest increase in locomotion speed as observed in Figure 4D. For low fields (0–20 mT), it is possible that the robot does not press hard enough on the rod to create strong, well-localized "anchors" in the contracted regions, so internal waves do not translate efficiently into net motion. As the field increases, the normal force between the robot and the rod in the contracted zones also increases, strengthening the effective "anchors." Beyond a certain limit (80 mT), the normal force at the "anchors" is already saturated and further increase in speed was not observed. Overall, the highest mean speed observed was 33.45 mm min^{-1} which was for 70 mT field strength at 5 Hz and which corresponds to approximately 1.1 body lengths min^{-1}. Therefore, for further experiments, 70 mT field strength was used for further investigations of robot behavior.

Apart from 6 mm rods, 4, 5, and 7 mm rods fabricated by the same material (Biomed Clear) were also tested to investigate the range of diameters for successful peristaltic locomotion (Movie S1). Rods of 7 mm diameter, nearly matching the robot's internal diameter of 7 mm, resulted in no observable locomotion, as the limited clearance prevented sufficient deformation and radial contraction of the robot and thus failed to generate peristaltic waves. In contrast, rods of 5 and 4 mm diameters also failed to produce locomotion, with the robot exhibiting rotation following the magnetic field rather than peristaltic anchoring and propagation. This asynchronous behavior arises because the reduced normal force and contact area in these configurations prevents the establishment of sufficiently strong, localized "anchors" in the contracted regions. Therefore, 6 mm rod diameter proved to be an optimal compromise to provide sufficient deformation and strong anchor points for peristalsis.

The untethered soft robot proved also capable of leveraging peristalsis to navigate inside a narrow hollow lumen (with internal diameter 1 mm larger than the robot structure) made out from the same Biomed Clear material as the rod (Figure 5A and Movie S2). Once again, locomotion speed was observed to increase with increasing rotating magnetic field frequency (Figure 5B) as higher frequency generates greater net displacement per unit time. In this case also the speed does not double (or triple) by doubling (or tripling) the frequency and remains slightly lower as predicted by Tanaka et al. [36]. The highest mean speed observed was 124.17 mm min^{-1} (applied field: 70 mT at 5 Hz) corresponding to approximately 4.1 body lengths min^{-1}. Additionally, when the robot moves within a narrow lumen, the robot is free to deform more in response to the applied magnetic field. This is in contrast to the case when the robot moves on a cylindrical rod, where the presence of the rigid rod limits the deformations that the robot can achieve in response to the external magnetic field. Consequently, the robot moving within the narrow lumen achieves a higher speed (Figure 5) compared to the case of movement over the rod (Figure 4). Apart from 10 mm lumen, 11 and 12 mm lumina fabricated again by BiomedClear were also tested. We found that the robot shows asynchronous behavior resulting in unpredictable movement, due to reduced normal force which generates weak anchor points (Movie S1).

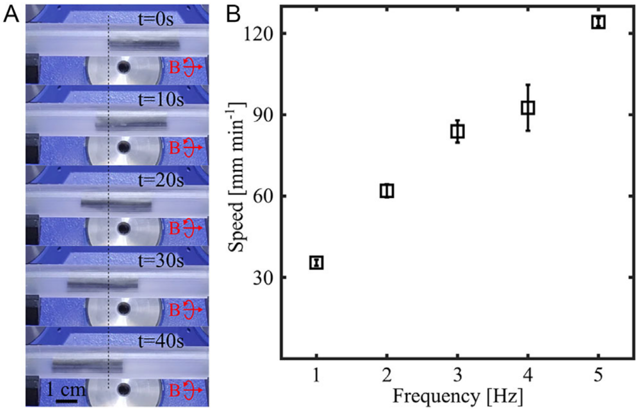

FIGURE 5 | Linear locomotion of the peristaltic robot in a BiomedClear lumen of 10 mm diameter under rotating magnetic fields (70 mT, 1 Hz). (A) Timestamped sequence of images showing the steady movement of the robot in the BiomedClear lumen. (B) Comparison of the speed of the robot inside the lumen with different rotational frequencies of the magnetic field at 70 mT field strength ($N = 5$).

The robot ability to exploit peristalsis to navigate into narrow lumina under rotating magnetic fields could enable several real-world applications. As proof of concept, we showed how the robot could reach a target point featured by a structural discontinuity (i.e., a gap), exploit peristalsis to overcome the gap, and continue its movement forward or reconnect the lumen for allowing fluid transport (Figure 6). The robot was actuated within a hollow flexible lumen whose internal diameter (9.6 mm) was just slightly bigger than the diameter of the robot (9 mm), propelling itself forward using peristaltic motion (70 mT, 3 Hz). Upon reaching the discontinuity in the lumen, the robot continued its propulsion into the adjacent, axially aligned lumen, effectively overcoming the gap (up to 9 mm) between the two structures. At this point, the robot could continue its locomotion forward or act as a bridge between the two lumina. Upon fluid injection, the robot could help fluid transport thus allowing discontinuity bridging. This capability is supported by the soft nature of the robot and by the adhesion between the flexible lumen and the robot external surface. Notably, a perfect match between the outer diameter of the robot and the inner diameter of the lumen is not desirable as such a condition could substantially hinder the peristaltic locomotion of the robot. Instead, the soft robot under current experimental conditions enables peristaltic locomotion while maintaining sufficient conformity to the lumen wall to support fluid transport. When water flow is initiated, it quickly fills any small interfacial voids between the robot wall and the flexible lumen, and no visible leak is observed during operation (Movie S3).

2.3 | Cargo Transport

The transport capabilities of the peristaltic robot were demonstrated with two types of cargo: a cylindrical rod and a spherical

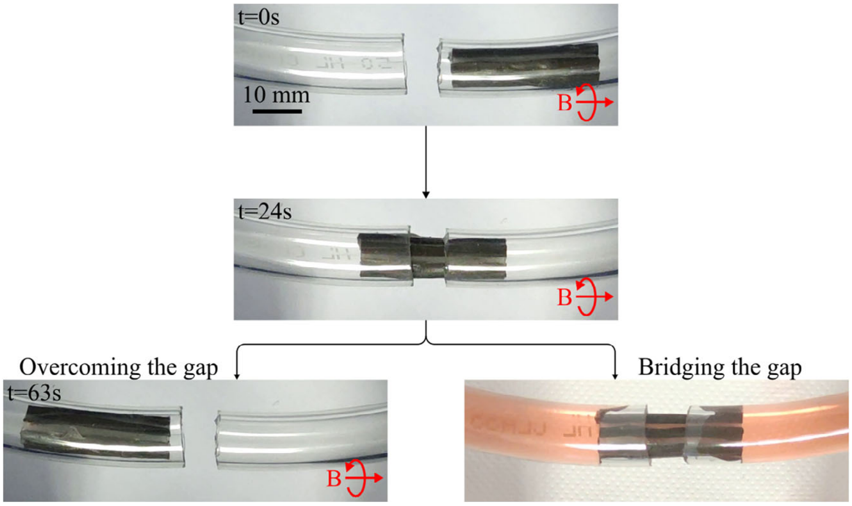

FIGURE 6 | Overcoming and bridging gaps in lumen with the peristaltic robot. Scale bar: 10 mm.

bead. For the cylindrical cargo, a 3D-printed solid rod (4 mm diameter, 90 mm length) was inserted through the hollow lumen of the robot fixed at one end to prevent its translation or rotation. Magnetic fields induced peristaltic locomotion, enabling the successful transport of the rod (Figure 7A and Movie S4). The rod diameter (4 mm) is smaller than the robot's internal diameter (about 7 mm), so the robot does not form a tight grip. Instead, the rod remains relatively free, bringing the friction-reducing model into play. Therefore, the peristaltic wave advances along the body and the rod translates in the opposite direction to the wave, as predicted for transport inside a fixed peristaltic channel [36]. The rod transport speed was found to be 7.85 ± 0.69 mm min^{-1} when the rod was transported towards the fixed end. However, a reduced speed of 3.27 ± 1.18 mm min^{-1} was observed when the rod was transported away from the fixed end. This speed asymmetry is a direct result of the mechanical asymmetry introduced by fixing one end of the robot, which constrains deformation and alters the frictional interaction at that end relative to the free end. This end-to-end difference modulates the effective anchoring pattern along the body, producing direction-dependent locomotion efficiency. For the spherical cargo, a 3D-printed rigid ball (6 mm diameter) was placed close to one end of the fixed robot. When actuated by rotating magnetic fields (70 mT, 1 Hz), the robot transports the ball to its free end (Figure 7B and Movie S5). As the constriction propagated, each passing contraction locally trapped the bead and advanced it stepwise along the lumen until it exited at the free end.

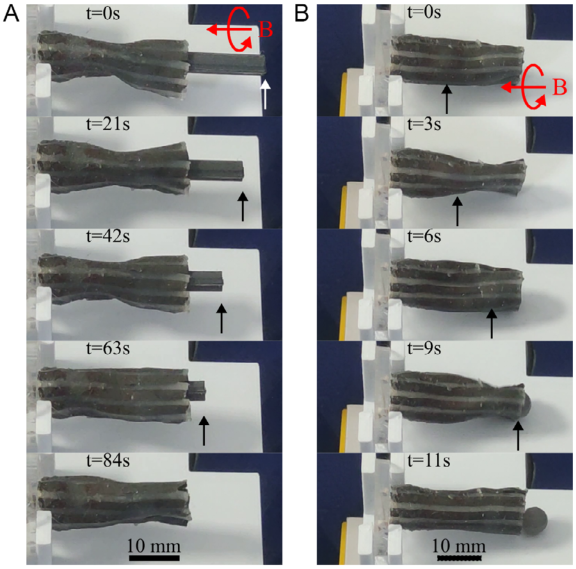

FIGURE 7 | Example transportation capabilities of the robot under rotating magnetic fields. (A) A 90 mm long 4 mm diameter cylindrical cargo transported within its lumen and (B) a 6 mm 3D printed spherical cargo transported to its open end with a continually rotating magnetic field. Scale bars: 10 mm.

Robot responsiveness to magnetic fields could be further exploited to perform locomotion through other mechanisms, such as rolling. If the robot is free to rotate, as in the case when the robot is lying on a flat surface, a rotating magnetic field induces robot rolling. In this case, the robot can be conceived as a single magnetic dipole moving uniformly and covering longer distances while eventually carrying a cargo. This versatility significantly expands the range of possible applications for the proposed system. To demonstrate this capability, the robot was used to guide a rigid cylindrical rod (6 mm) to a target where a sticky glue (Silpoxy, Smooth-On) automatically held the cargo. Since both the robot and the cargo were free to move, the robot demonstrated rolling behavior under rotating magnetic fields (Figure 8A,B). Once the cargo was in place, rotating magnetic fields were used to move the robot away from the cargo using peristalsis and then to roll it further away (Figure 8C,D). This result showcases the robot ability to seamlessly integrate both locomotion and transport, demonstrating its adaptability for diverse functional scenarios (Movie S6). The permanent magnet used for actuation (>20 mT) was placed under the robot when it was in the position shown in Figure 8A for rolling the cargo to the target, and moved to under the robot when it was in the position shown in Figure 8B for the rest of the demonstration. Since the magnetic fields applied for this demonstration were generated by a permanent magnet, uniform magnetic fields could not be generated and magnetic gradients also inevitably come into play which deform the robot slightly.

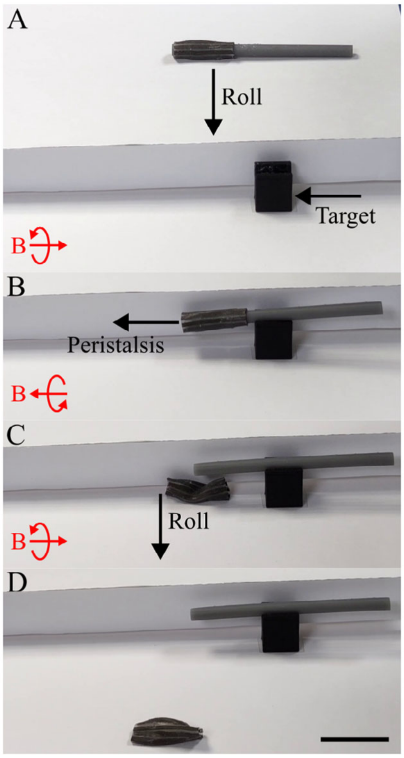

FIGURE 8 | Transportation of a rigid cylindrical load to a target by the robot and then moving away from it. (A) The robot rolls the rod towards the target where it gets stuck due to the presence of sticky glue. (B) The robot then translates over the rod till the rod is completely out of the robot and then (C,D) the robot rolls away. Scale bar: 3 cm.

3 | Conclusions

In this paper we reported an untethered, lightweight, magnetic soft robot leveraging peristalsis both to locomote in different environments and transport cargo within itself. In this direction, the results reported in this manuscript represent a significant step forward with respect to the state of the art in terms of multifunctionality and output performance.

By looking at traditional actuation strategies typically employed in soft and bioinspired robotics, it is evident how the proposed tendon-driven and pneumatic peristaltic robots typically have sizes in the range of tens of centimeters [12, 13, 15, 16, 19, 20]. The presence of tendons and tubing makes further miniaturization challenging. In contrast, the peristaltic robot presented in this work is at the centimeter scale, enabled by magnetic actuation, which eliminates the need for onboard connections, thus making the principle easily scalable. While SMA based peristaltic robots have also been demonstrated [9, 10], these designs are not fully untethered either, generally requiring electrical wiring and onboard heating elements. Similarly, piezoelectric [22] and light-based [25] solutions still depend on tethers or direct line of sight. In contrast, the robot demonstrated in this paper operates in a fully untethered manner, driven solely by externally controlled magnetic fields.

The use of magnetic fields as an actuation strategy for both locomotion and transport offers also interesting potentialities in terms of workspace. Due to the programmed magnetization profile embodied in the peristaltic robot structure, the remote magnetic fields employed for actuation are easy to control and suitable also for large-scale workspaces. Most of the demonstrations in this work were performed within the workspace of a commercial electromagnetic field generator which has high controllability but also a limited operational range, as the strength of the applied field decreases with distance from the source. However, the workspace can potentially be significantly enlarged by using a simple rotating permanent magnet as demonstrated in Figure 8 and Movie S6, thereby expanding the reach of such robots.

We also proved that the shift to an untethered multifunctional design with potentialities in terms of size, weight and workspace scaling did not cause a deterioration in the locomotion performance, if compared with the state of the art. The maximum locomotion speed demonstrated by our peristaltic robot is 4.1 body lengths min^{-1} (70 mT at 5 Hz). This exceeds the speeds reported for SMA-based peristaltic robots, which range from 0.4 to 1.5 body lengths min^{-1} [9, 10], and pneumatic robots, which achieve only 0.1–0.21 body lengths min^{-1} [13,14]. While the softworm reported by Menciassi et al. [11] shows a slightly higher speed up to 6 body lengths min^{-1}, it also presents several limitations compared with the proposed design. Its weight is significantly higher (3.8 kg vs. 0.95 g for our robot), and it relies on a motor-driven mechanically complex architecture with numerous cable-driven hoop actuators. As a result, the overall structure is relatively bulky and difficult to miniaturize, limiting its applicability in constrained environments. Furthermore, the speed of the robot demonstrated here can be further increased by optimizing the magnetic field strength and frequency combination beyond what was attainable with our commercial electromagnetic field generator.

Our robot is demonstrated to move over cylindrical rods, inside narrow lumina, and across discontinuities in lumina. The relative direction of motion between an object and the robot depends on the contact mechanics, friction, and force transmission between the two. By carefully controlling these interactions, peristaltic robots can be optimized for different applications, whether for locomotion or transporting objects internally. For our experimental conditions, rod diameters approximately 15% smaller than the internal diameter of the robot and lumen diameters approximately 7%–11% larger than the outer diameter of the robot act as ideal conditions for locomotion. The peristaltic robot ability to move over solid rods and within narrow lumina has significant potential medical and industrial applications. The unique combination of soft compliance, untethered magnetic actuation, and peristaltic locomotion makes the proposed robot particularly well suited for operation in constrained and delicate environments where conventional rigid robotic systems face limitations. In minimally invasive medicine, the robot could support guidewire- and catheter-based interventions by autonomously traversing vascular or luminal pathways of suitable diameters while reducing contact forces, minimizing the risk of tissue trauma and limiting any breaking issues. Unlike conventional push-based catheter navigation, the distributed peristaltic propulsion mechanism can improve mobility in tortuous geometries and across partially discontinuous pathways while maintaining stable contact with surrounding structures. Its hollow cylindrical architecture additionally enables the transport or deployment of therapeutic payloads, miniature surgical tools, stents, or sensing elements through confined anatomical pathways, which could potentially help in medical implants positioning. Beyond biomedical applications, the robot's ability to locomote over rods, traverse narrow tubing, bridge gaps, and transport internal payloads could enable inspection, maintenance, or temporary repair operations in chemical, pharmaceutical, or other industrial pipeline and tubing networks, particularly in environments where tethered or rigid systems have limited accessibility. Furthermore, the fully soft structure and relatively simple jig-assisted fabrication strategy provide a low-cost and mechanically robust platform that could be adapted to application-specific geometries and scales.

4 | Experimental Section

4.1 | Experimental Design

The primary objective of this study was to investigate how a hollow, magnetically actuated peristaltic soft robot can generate and modulate peristaltic locomotion on cylindrical rods and inside lumina. The dependency of locomotion on peristaltic wave frequency, actuation amplitude, and the region of anchoring along the robot body was also to be investigated. Another objective was to demonstrate that the same peristaltic robot can be used to transport internal cargo of different geometries through the robot lumen.

To address these objectives, the study was designed around five modeling and experimental tasks. First, the behavior of single actuation units was studied through torsion simulations and corresponding validation through torsion experiments under actuating magnetic fields to confirm their spiral magnetization profile. Second, multiple actuation units were simulated to demonstrate that such combinations could enable the robot to exhibit peristalsis. This model was subsequently confirmed through experiments. A good overlap between simulated and

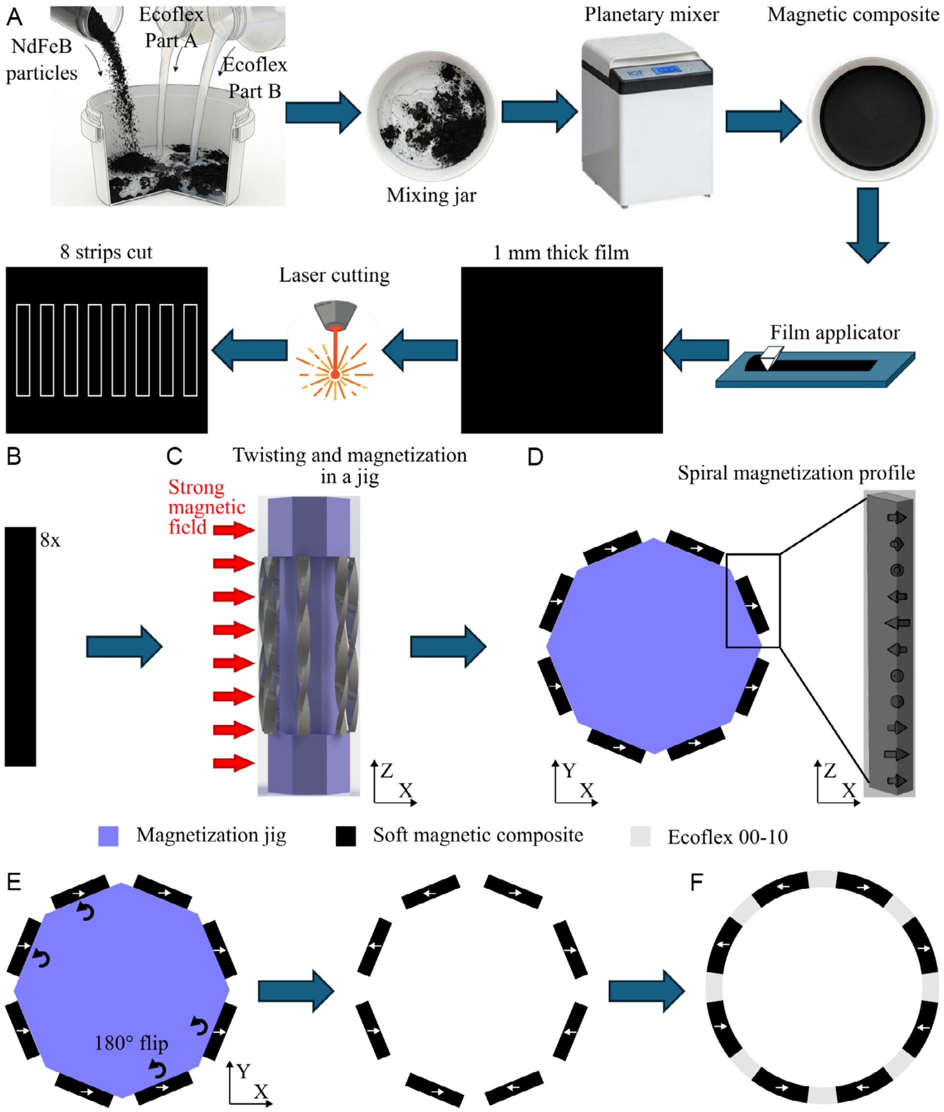

FIGURE 9 | Fabrication of the peristaltic robot. (A) The magnetic composite was prepared by mixing equal weights of Ecoflex 00-10 and NdFeB particles in a planetary mixer. A 1 mm thick film of this composite was produced using a film stretcher and a laser cutter was used to cut 8 strips of the composite. (B–D) These 8 strips of the magnetic composite in required dimension were given one full twist and fixed to a magnetization jig and magnetized resulting in a spiral magnetization profile in each of them. (E) 4 of the strips as shown were flipped by 180° and all of them were bonded together with Ecoflex 00-10 which also acted as spacers between them to produce (F) the final robot.

experimental behavior was achieved across both the single actuation unit level and the multiunit peristaltic robot. Third, locomotion experiments were performed with the robot crawling over 6 mm diameter rigid rods fabricated from different materials—BiomedClear resin (Formlabs), PET-G (Polyethylene Terephthalate—Glycol), and PLA (Polylactic Acid), in order to test whether peristaltic locomotion is robust to changes in substrate material while the geometric constraint (rod diameter) is held fixed. Fourth, parametric actuation studies were carried out by systematically varying the strength (10–80–mT) and frequency (1–5 Hz) of spatially uniform rotating magnetic fields to quantify how the robot speed depends on the applied field features. Finally, cargo-transport experiments were carried out to examine peristaltic transport of cylindrical rods inserted through the lumen and spherical beads placed inside the lumen near one end, with the robot itself fixed, to test how peristaltic constrictions can move objects placed in the inner cavity.

4.2 | Robot Prototyping

The preparation of the soft magnetic composite and the required strips from it is described in Ilaria et al. [37]. The soft magnetic composite was made by embedding NdFeB particles (MQFP-15-7, Magnequench) in Ecoflex 00-10 silicone (Smooth-On) at a 1:1 weight ratio (Figure 9A). A 1-mm thick film was prepared from the uncured composite using a film stretcher (TQC Sheen), from which strips of desired dimensions were cut. Eight 30 × 2 mm strips (Figure 9B) were twisted once (rotation by 360°) and attached to the faces of a magnetization jig shaped as an octagonal prism (Figure 9C). A strong magnetic field (1.9 T) was applied along a diagonal of the octagonal cross-section along the entire length using a Vibrating Sample Magnetometer (EZ7, Microsense) to magnetize the strips. Once removed from the jig, the strips were untwisted and returned to their rest state, featuring a spiral magnetization profile along the -Z axis (Figure 9D). Four of the strips were rotated 180° (Figure 9E,F) while maintaining the orientation of the remaining four, and all eight strips were bonded together using Ecoflex 00-10, which also served as spacer among adjacent strips, to assemble the robot with an aspect ratio 3.3 (length: 30 mm, outer diameter: 9 mm, Figure 1).

4.3 | Numerical Modeling

A single actuation unit and the complete robot were numerically modeled in COMSOL Multiphysics using Solid Mechanics and Magnetic Fields interfaces. The single actuation unit was modeled as a hyperelastic material using a three-term Ogden formulation to accurately capture its torsional deformation under magnetic actuation. The Ogden parameters were obtained by fitting the stress–strain data of the corresponding material. For the full robot model, the eight magnetized strips were assigned the same hyperelastic material model and Ogden parameters as those used for the single actuation unit, while the non-magnetic Ecoflex 00-10 spacer regions were modeled with the same three-term Ogden formulation but with a different parameter set calibrated from tests on pure Ecoflex 00-10. All Ogden parameters used in the simulations are listed in Table S2.

The magnetic fields applied in the simulations were static and spatially uniform. The interaction between the applied magnetic field $\boldsymbol{B}$ and the magnetization $\boldsymbol{M}$ was implemented using an equivalent tangential-stress formulation, as developed in previous studies [34, 35]. In this approach, the distributed magnetic torque is represented as opposing surface stresses on the boundaries of each strip. The full derivation and numerical implementation of this torque-mapping method are provided in Supporting Information (Modeling a single twisting unit and Modeling the full robot).

For both the single unit and robot models, one end of each structure was fixed, and the remaining body was allowed to deform quasi-statically under the magnetic fields. Model predictions were validated by comparing the twist angle (single unit) and robot deformation and constriction length (full robot) with experimental measurements.

4.4 | Experimental Validation

The fabricated robot was actuated in the Octomag system (Magnebotix, Switzerland)—a commercial 8-coil magnetic field generator. Octomag has a spherical workspace with 5 cm diameter. To extend the workspace, the demonstration in Movie S6 is carried out using a cylindrical N35 NdFeB (Neodymium Iron Boron) permanent magnet (6 cm in diameter and 7 cm in length) mounted on a robotic arm (Melfa RV-3S, Mitsubishi, Japan). Robot locomotion videos were recorded using a commercial phone camera (Mi 10T Pro, Xiaomi), and the Computer Vision Toolbox in MATLAB (MathWorks) was utilized to track the robot with virtual markers.

4.5 | Statistical Analysis

For the locomotion demonstrations, the speed values reported are the mean and standard deviation of 5 repetitions on the same sample.

Author Contributions

Conceptualization: Mohammad Hasan Dad Ansari, Linda Paternò, Veronica Iacovacci and Arianna Menciassi. Methodology: Mohammad Hasan Dad Ansari, Linda Paternò, Chenjun Wu and Veronica Iacovacci. Investigation: Mohammad Hasan Dad Ansari, Chenjun Wu and Veronica Iacovacci. Visualization: Mohammad Hasan Dad Ansari and Chenjun Wu. Funding acquisition: Arianna Menciassi. Supervision: Linda Paternò, Veronica Iacovacci and Arianna Menciassi. Writing – original draft: Mohammad Hasan Dad Ansari, Linda Paternò and Chenjun Wu. Writing – review & editing: Mohammad Hasan Dad Ansari, Linda Paternò, Chenjun Wu, Veronica Iacovacci and Arianna Menciassi.

Acknowledgements

Open access publishing facilitated by Scuola Superiore Sant'Anna, as part of the Wiley - CRUI-CARE agreement.

Funding

This work was supported by the European Project MAPWORMS – Mimicking Adaptation and Plasticity in WORMS Grant Agreement

101046846 (https://www.mapworms.eu) and the European Commission under the Horizon Europe program (REGO Project, Grant #101070066).

Conflicts of Interest

The authors declare no conflicts of interest.

Data Availability Statement

The data that support the findings of this study are available from the corresponding author upon reasonable request.

References

1. J. Rubenson, and G. S. Sawicki, "Running Birds Reveal Secrets for Legged Robot Design," *Science Robotics* 7 no, (64), 2022): https://doi.org/10.1126/scirobotics.abo2147.

2. D. J. Todd, "Chapter 2: A Brief History of Walking Machines," *in Walking Machines: An Introduction to Legged Robotics* (Springer, 2012), ISBN: 978-1-4684-6860-1.

3. D. Chen, Z. Wu, Y. Meng, M. Tan, and J. Yu, "Development of a High-Speed Swimming Robot With the Capability of Fish-Like Leaping," *IEEE/ASME Transactions on Mechatronics* 27 (2022): 3579–3589, https://doi.org/10.1109/TMECH.2021.3136342.

4. X. Zhou, X. Wen, Z. Wang, et al., "Swarm of Micro Flying Robots in the Wild," *Science Robotics* 7 (2022): eabm5954, https://doi.org/10.1126/scirobotics.abm5954.

5. W. E. Garrey, and A. R. Moore, "Peristalsis and Coordination in the Earthworm," *American Journal of Physiology-Legacy Content* 39 (1915): 139–148, https://doi.org/10.1152/ajplegacy.1915.39.2.139.

6. J. G. Brasseur, "A Fluid Mechanical Perspective on Esophageal Bolus Transport," *Dysphagia* 2 (1987): 32–39, https://doi.org/10.1007/BF02406976.

7. W. B. Cannon, "The Nature of Gastric Peristalsis," *American Journal of Physiology-Legacy Content* 29 (1911): 250–266, https://doi.org/10.1152/ajplegacy.1911.29.2.250.

8. J. D. Huizinga, "Gastrointestinal Peristalsis: Joint Action of Enteric Nerves, Smooth Muscle, and Interstitial Cells of Cajal," *Microscopy Research and Technique* 47 (1999): 239–247, https://doi.org/10.1002/(SICI)1097-0029(19991115)47:4<239::AID-JEMT3>3.0.CO;2-0.

9. A. Menciassi, S. Gorini, G. Pernorio, and P. Dario, "A SMA Actuated Artificial Earthworm," in IEEE International Conference on Robotics and Automation (ICRA), (2004), 3282–3287.

10. S. Seok, C. D. Onal, K.-J. Cho, R. J. Wood, D. Rus, and S. Kim, "Meshworm: A Peristaltic Soft Robot With Antagonistic Nickel Titanium Coil Actuators," *IEEE/ASME Transactions on Mechatronics* 18 (2013): 1485–1497, https://doi.org/10.1109/TMECH.2012.2204070.

11. C. Kazoleas, J. Zhang, and S. Yuan, "Tensiworm: A Novel Tensegrity Robot With Enhanced Peristaltic Locomotion Efficiency," in 2025 IEEE International Conference on Robotics and Automation (ICRA), (2025), 11645–11652.

12. A. S. Boxerbaum, K. M. Shaw, H. J. Chiel, and R. D. Quinn, "Continuous Wave Peristaltic Motion in a Robot," *The International Journal of Robotics Research* 31 (2012): 302–318, https://doi.org/10.1177/0278364911432486.

13. K. A. Daltorio, A. S. Boxerbaum, A. D. Horchler, K. M. Shaw, H. J. Chiel, and R. D. Quinn, "Efficient Worm-Like Locomotion: Slip and Control of Soft-Bodied Peristaltic Robots," *Bioinspiration & Biomimetics* 8 (2013): 035003, https://doi.org/10.1088/1748-3182/8/3/035003.

14. D.-J. Zhang, B.-J. Qiu, B. Li, and Y. Yang, "Design and Experimental Study of a Biomimetic Earthworm-Like Peristaltic Robot Mechanism," *Advances in Mechanical Engineering* 17 (2025): 16878132251382727, https://doi.org/10.1177/16878132251382727.

15. R. Okuma, Y. Naruse, F. Ito, and T. Nakamura, "Peristaltic Soft Robot for Long-Distance Pipe Inspection With an Endoskeletal Structure for Propulsion and Traction Amplification," in 2024 IEEE/RSJ International Conference on Intelligent Robots and Systems (IROS), (2024), 4053–4060.

16. R. Das, S. P. M. Babu, F. Visentin, S. Palagi, and B. Mazzolai, "An Earthworm-Like Modular Soft Robot for Locomotion in Multi-Terrain Environments," *Scientific Reports* 13 (2023): 1571, https://doi.org/10.1038/s41598-023-28873-w.

17. Q. Han, J. Xu, S. He, S. Kang, and L. Li, "Design and Actuation of a Rigid-Soft Coupled Pneumatic Peristaltic Robot for Pipeline Environments," *IFAC-PapersOnLine* 59 (2025): 1605–1610, https://doi.org/10.1016/j.ifacol.2025.11.387.

18. G. Li, M. Wang, Y. Zhu, and Y. Wang, "Development of a Leech-Inspired Peristaltic Crawling Soft Robot for Intestine Inspection," *International Journal of Intelligent Robotics and Applications* 8 (2024): 878–888, https://doi.org/10.1007/s41315-024-00358-7.

19. Y. Peng, H. Nabae, Y. Funabora, and K. Suzumori, "Peristaltic Transporting Device Inspired by Large Intestine Structure," *Sensors and Actuators A: Physical* 365 (2024): 114840, https://doi.org/10.1016/j.sna.2023.114840.

20. S. Uzawa, H. Kumamoto, C. Yamazaki, M. Okui, and T. Nakamura, "Development of Peristaltic Transfer System to Transport Feces in Space: Proposal of Driving Method Using Pressure Difference in Peristaltic Pump," *IEEE Access* 10 (2022): 128399–128407, https://doi.org/10.1109/ACCESS.2022.3227068.

21. M. Su, B. Liang, H. Chen, et al., "A Bio-Inspired Intestine Robot Utilizing Soft Origami Kresling Structures to Imitate Peristaltic Wave Motion and Transport," *Biomimetic Intelligence and Robotics* 6 (2026): 100282, https://doi.org/10.1016/j.birob.2026.100282.

22. K. Nakahara, M. Yamamoto, Y. Okayama, K. Yoshimura, K. Fukagata, and N. Miki, "A Peristaltic Micropump Using Traveling Waves on a Polymer Membrane," *Journal of Micromechanics and Microengineering* 23 (2013): 085024, https://doi.org/10.1088/0960-1317/23/8/085024.

23. Y. Hou, L. He, D. Hu, L. Zhang, B. Yu, and G. Cheng, "Recent Trends in Structures and Applications of Valveless Piezoelectric Pump—A Review," *Journal of Micromechanics and Microengineering* 32 (2022): 053002, https://doi.org/10.1088/1361-6439/ac5c77.

24. L. Zhang, L. Chen, L. Xu, H. Zhao, R. Wen, and F. Xia, "Gastrointestinal-Peristalsis-Inspired Hydrogel Actuators for NIR-Controlled Transport of Viscous Liquids," *Advanced Materials* 35 (2023): 2212149, https://doi.org/10.1002/adma.202212149.

25. S. Palagi, A. G. Mark, and S. Y. Reigh, et al., "Structured Light Enables Biomimetic Swimming and Versatile Locomotion Of Photoresponsive Soft Microrobots," *Nature Materials* 15 (2016): 647–653, https://doi.org/10.1038/nmat4569.

26. M. H. D. Ansari, V. Iacovacci, and S. Pane, et al., "3D Printing of Small-Scale Soft Robots With Programmable Magnetization," *Advanced Functional Materials* 33 (2023): 2211918, https://doi.org/10.1002/adfm.202211918.

27. M. H. D. Ansari, X. T. Ha, M. Ourak, et al., "Characterization of a 3D Printed Endovascular Magnetic Catheter," *Actuators* 12 (2023): 409, https://doi.org/10.3390/act12110409.

28. J. Zhang, X. Bao, Z. Zhu, et al., "In Situ Mechanostimulation of Bio-hybrid Millirobots for Enhanced Cell Functionality and Delivery," *Science Advances* 12 (2026): eadx9616, https://doi.org/10.1126/sciadv.adx9616.

29. F. C. Landers, L. Hertle, V. Pustovalov, et al., "Clinically Ready Magnetic Microrobots for Targeted Therapies," *Science* 390 (2025): 710–715, https://doi.org/10.1126/science.adx1708.

30. Z. Yang, C. Xu, J. X. Lee, and G. Z. Lum, "Magnetic Miniature Soft Robot With Reprogrammable Drug-Dispensing Functionalities: Toward

Advanced Targeted Combination Therapy," *Advanced Materials* 36 (2024): 2408750, https://doi.org/10.1002/adma.202408750.

31. H. Wen, Z. Shao, Y. Sun, et al., "Magnetoactive Bistable Soft Actuators for Programmable Large Shape Transformations at Low Magnetic Fields," *Nature Communications* 16 (2025): 9714, https://doi.org/10.1038/s41467-025-64855-4.

32. S. Sharma, L. C. Jung, and N. Lee, et al., "Wireless Peristaltic Pump for Transporting Viscous Fluids and Solid Cargos in Confined Spaces," *Advanced Functional Materials* 34 (2024): 2405865, https://doi.org/10.1002/adfm.202405865.

33. J. Zhang, Z. Ren, W. Hu, et al., "Voxelated Three-Dimensional Miniature Magnetic Soft Machines via Multimaterial Heterogeneous Assembly," *Science Robotics* 6 (2021): eabf0112, https://doi.org/10.1126/scirobotics.abf0112.

34. C. Wu, Y. Xiang, S. Qu, Y. Song, and Q. Zheng, "Numerical Study of Millimeter-Scale Magnetorheological Elastomer Robot for Undulatory Swimming," *Journal of Physics D: Applied Physics* 53 (2020): 235402, https://doi.org/10.1088/1361-6463/ab795f.

35. C. Wu, and J. Yang, "Magnetically Actuated Soft Small-Scale Robot for Undulating Swimming," *Physics of Fluids* 37 (2025): 042025, https://doi.org/10.1063/5.0264321.

36. Y. Tanaka, K. Ito, T. Nakagaki, and R. Kobayashi, "Mechanics of Peristaltic Locomotion and Role of Anchoring," *Journal of the Royal Society Interface* 9 (2012): 222–233, https://doi.org/10.1098/rsif.2011.0339.

37. I. Cedrola, S. Maglio, M. H. D. Ansari, A. Menciassi, and L. Paternò, "Magnetically-Driven Deployable Structure Inspired by Worms," *Bioinspiration & Biomimetics* 21 (2026): 036007, https://doi.org/10.1088/1748-3190/ae6698.

Supporting Information

Additional supporting information can be found online in the Supporting Information section.